metals

MDPI

Article

Effect of Applied Tensile Stress on Hydrogen-Induced Delayed Fracture Mode of Fe-Ni-Cr Austenitic Alloy Weldment

Yingjie Yan [1,2,*], Yukun Zhang [1,2], Lixian Zhao [1,2], Yongqing Chen [1,2], Rui Cao [1,2], Honghui Wu [3,*], Yang He [3,*], Yu Yan [4] and Lijie Qiao [3,4,*]

[1] State Key Laboratory of Advanced Processing and Recycling of Nonferrous Metals, Lanzhou University of Technology, Lanzhou 730050, China
[2] School of Materials Science and Engineering, Lanzhou University of Technology, Lanzhou 730050, China
[3] Beijing Advanced Innovation Center for Materials Genome Engineering, University of Science and Technology Beijing, Beijing 100083, China
[4] Corrosion and Protection Center, Key Laboratory for Environmental Fracture (MOE), University of Science and Technology Beijing, Beijing 100083, China
* Correspondence: yjyan@lut.edu.cn (Y.Y.); wuhonghui@ustb.edu.cn (H.W.); yanghe@ustb.edu.cn (Y.H.); lqiao@ustb.edu.cn (L.Q.)

Abstract: Fe-Ni-Cr austenitic alloys are widely used in hydrogen environments as structural materials. Their weld normally shows higher hydrogen-embrittlement sensitivity than the base metal, endangering large-scale applications. Herein, by using electron microscopy and numerical calculations, the influence of applied load on the fracture mode of hydrogen-embrittled JBK-75 alloy weldment is revealed and correlated with a competition between hydrogen-prompted intergranular decohesion (HPID) and hydrogen-enhanced localized plasticity (HELP). Therefore, independent of the load levels, the weld featuring a lower strength and smaller grain sizes is always more vulnerable to hydrogen embrittlement than the base metal.

Keywords: Fe-Ni-Cr alloy; weldment; applied tensile stress; hydrogen-induced delayed fracture mode

Citation: Yan, Y.; Zhang, Y.; Zhao, L.; Chen, Y.; Cao, R.; Wu, H.; He, Y.; Yan, Y.; Qiao, L. Effect of Applied Tensile Stress on Hydrogen-Induced Delayed Fracture Mode of Fe-Ni-Cr Austenitic Alloy Weldment. *Metals* **2022**, *12*, 1614. https://doi.org/10.3390/met12101614

Academic Editors: Francesco Iacoviello and João Pedro Oliveira

Received: 10 August 2022
Accepted: 21 September 2022
Published: 27 September 2022

1. Introduction

Hydrogen-induced delayed fracture involves hydrogen-defect interactions at multiple-length scales, and usually occurs in transition metals under the combined action of hydrogen and applied tensile stress [1]. Metallurgical factors [2,3], microstructure [4,5], hydrogen content [6–8], and strain rate [9–12] all affect the hydrogen-induced delayed fracture mode of advanced metal materials. For the high-strength steels that display intergranular failure, hydrogen-induced delayed fracture has been attributed to decohesion caused by hydrogen segregation at grain boundaries [13]. Whereas for others that display transgranular failure, it has been associated with a weakening effect in the presence of hydrogen [14,15].

With high strength, excellent corrosion resistance, and low hydrogen embrittlement sensitivity, Fe-Ni-Cr precipitation-strengthened austenitic alloys (e.g., JBK-75) are widely used in superchargers, gas turbine jet engines, and hydrogen storage tanks [16–19]. Using high-temperature aging treatment, coherent precipitates γ' (Ni_3(Al, Ti)) are formed in these alloys and strengthen the material by retarding dislocation slip. In large-scale applications, the electron-beam welding (EBW) technique is usually used to joint these alloys. EBW provides high penetration depth, less contamination, and narrow heat-affected zone [20–22]. However, like many other welding techniques [23–26], EBW also generates a microstructure that differs from the base metal and can be vulnerable to harsh service environments [27,28]. Compared with the equiaxed grains of the base metal, the weld is fine columnar grains, and the γ' in the weld is an inhomogeneous distribution after post-weld aging treatment [29,30]. The larger size and more dispersed γ' in the weld results in lower strength and hardness than the base metal [31].

When the modified -JBK75 alloy weldment is used as a high-pressure hydrogen storage tank, it usually bears high constant tensile stress from internal H_2 during service. In the process of evaluating the service safety of modified -JBK75 alloy weldment as a high-pressure hydrogen storage tank, hydrogen-induced delayed fracture always occurs at the weld and the normalized threshold stress decreases exponentially with an increase in the closing time t_c [32]. Notably, it has been found that the magnitude of the constant tensile stress significantly affected the hydrogen-induced delayed fracture mode of the weld. This indicates that the weakness of the weld is variant with different service stresses, which is critical for further improving the weld performance.

However, the effect of the magnitude of the constant tensile stress on the hydrogen-induced delayed fracture mode is still missing. Herein, constant tensile stress tests with dynamic hydrogen-charging are carried out to simulate the service condition. Scanning electronic microscopy is employed to analyze the detailed fractography. Transmission electron microscopy is used to characterize the dislocation activities. Moreover, the hydrogen distribution contours of the specimens at the fracture time are quantitatively evaluated using finite element simulation. Finally, the effect of the magnitude of constant tensile stress on the hydrogen-induced delayed fracture mode are clarified.

2. Experiments

The chemical composition of precipitation-strengthened Fe-Ni-Cr austenitic alloy, i.e., modified -JBK75 alloy, is shown in Table 1. The alloy plates were quenched in water after solution treatment at 1253 K for 1 h. Then, two plates were full-penetration butt-welded in a vacuum electron-beam welding apparatus (Institute of Metal Research, Chinese Academy of Sciences, Shenyang, China). The full-penetration butt-welding process was conducted in a vacuum electron-beam welding apparatus using 60 kV and 20 mA current at a welding speed of 100 cm/min. Finally, the weldment was aged at 1013 K for 8 h to eliminate internal stress and to obtain near peak-aged γ' precipitates, followed by cooling in air.

Table 1. Chemical composition (wt.%) of the precipitation-strengthened Fe-Ni-Cr austenitic alloy that was used in this study.

Element	Mn	C	Si	V	Al	Mo	Ti	Cr	Ni	Fe
Content	Minimize	$\leq$0.02	0.2	0.25	0.3	1.3	2.1	15	31	Balance

A small weldment specimen was then polished and etched in 50% aqua regia glycerol etchant for 3 min. The microstructures of the base metal and the weld are shown in Figure 1. The weld width is about 1.5 mm. The microstructure of the base metal is typical austenite with an average grain size of about 45 µm and some annealing twins. The weld is cast microstructure. There is no heat-affected zone, with large grains near the weld/base metal interface.

The transmission electron microscopy (Japan Electronics Co., Ltd., Tokyo, Japan) characterizations show that the base metal and weld are both austenite, as shown in Figure 2. There are some complex precipitates of about 200 nm in the weld, and the dislocation density is much higher than the base metal. The effect of microstructures on the hydrogen embrittlement of the weldment has also been discussed systematically [31,32].

In order to evaluate the effect of the applied constant tensile stress on the hydrogen-induced delayed fracture mode of the weldment, the tensile test of the hydrogen-free specimen was carried out at room temperature in air to obtain the engineering stress–strain curve at first. The specimens for the hydrogen-free tensile tests and the dynamic hydrogen-charged constant stress tensile tests were cut from the plate after aging. The weld line was positioned at the center of the specimens. The specimens were mechanically polished with 1200 mesh SiC abrasive paper. The schematic diagram of the tensile specimen is shown in Figure 3. Then, macroscopic tensile tests were carried out at room temperature in air to obtain stress–strain curve with a strain rate of 5×10^{-4}/s and the load direction perpendicular to the weld line. According to the engineering stress–strain curve of the hydrogen-free specimen, the stress applied in dynamic hydrogen-charging of constant tensile stress specimens was selected.

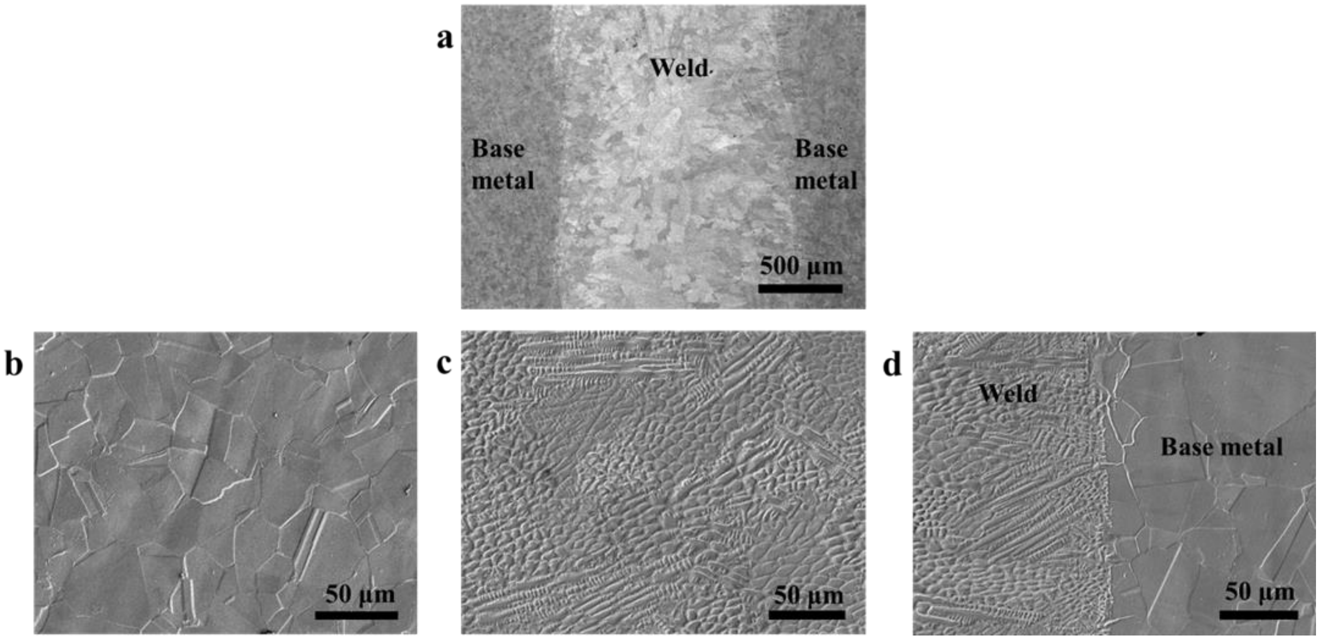

Figure 1. Microstructures of the weldment. (**a**) Macro morphology. (**b**) The base metal. (**c**) The weld. (**d**) The weld/base metal interface.

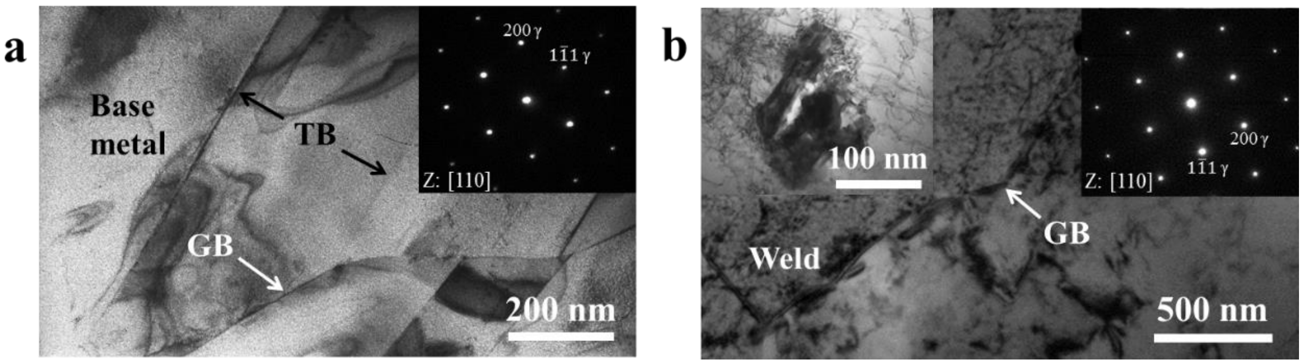

Figure 2. Transmission electron microscopy observation of the weldment. (**a**) The base metal, and (**b**) the weld, respectively. Upper right insert in (**a**) shows the electron diffraction pattern of the base metal. Upper left insert in (**b**) shows a complex precipitate in the weld. Upper right insert in (**b**) shows the electron diffraction pattern of the weld. GB: grain boundary, TB: twin boundary.

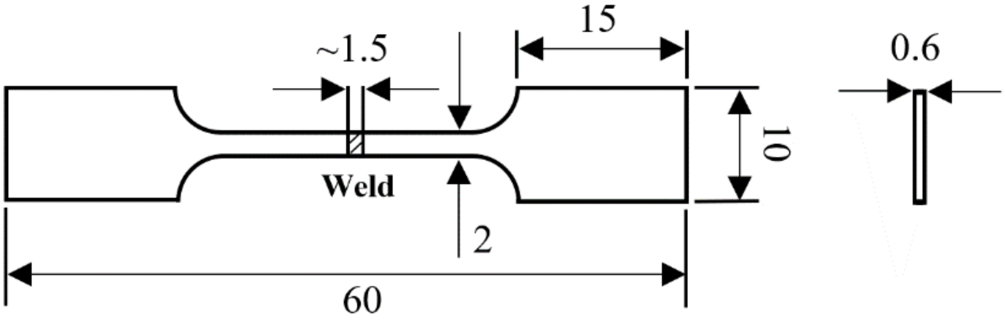

Figure 3. Schematic diagram of the tensile specimen (in mm).

As a hydrogen storage tank, the weldment usually bears a high level of constant stress from internal H_2. To simulate the service environment, the specimen shown in Figure 3 was electrochemically hydrogen-charged after being installed on the constant tensile stress experimental equipment, which was then slowly loaded to the predetermined tensile stress and held until fracture at room temperature. The specimen was hydrogen-charged at a current density of 400 mA/cm^2 in a solution containing 0.5 mol/L H_2SO_4 and 0.25 g/l As_2O_3 (an additive to prevent the recombination of hydrogen atoms during the electrolysis). After fracture, the strain levels of the specimens of dynamic hydrogen-charged constant stress tensile tests were roughly estimated based on the engineering stress–strain curve of the hydrogen-free specimen. The fracture surfaces were examined by using a scanning electron microscope.

In the finite element modeling, the hydrogen diffusion is governed by the classical diffusion equation:

$$\frac{\partial H(r,t)}{\partial t} = \nabla[D(H,r)\nabla H(r,t)] \quad (1)$$

where $H(r,t)$ is the hydrogen concentration of the specimens at location r and time t, $D(H,r)$ is the diffusion coefficient for hydrogen concentration H and at location r, and ∇ represents the vector differential operator. In the current work, the diffusion coefficient $D(H,r)$ is assumed to be isotropic, with a constant value of 1.07196×10^{-3} μm^2/s at room temperature without applied stress [33]. With applied stress, the material microstructure may change. Both the applied stress and the material microstructure change would change the diffusion coefficient to some extent. The finite element simulation is a semi-quantitative estimation of the hydrogen distribution.

3. Results

3.1. Marginal Hydrogen-Induced Brittle Fracture Zone

The engineering stress–strain curve of the hydrogen-free weldment specimen is shown in Figure 4a. The specimen fractured at the weld (Figure 4b), with a yield strength (YS) and the ultimate tensile strength (UTS) of 780 MPa and 1005 MPa, respectively. Similar to the hydrogen-free specimen, all of the hydrogen-induced delayed fractures of the dynamic hydrogen-charged constant stress tensile specimens took place within the weld (Figure 4c). As shown in prior work [32], the service time or hydrogen-induced delayed fracture time decreased with increasing constant tensile stress.

The fractured surfaces of the hydrogen-free weldment specimen are shown in Figure 5. The fractography of the hydrogen-free specimen exhibited obvious cross-section reduction with a typical dimple feature. No secondary crack was observed.

To evaluate the effects of applied stress, two groups of hydrogen-charged constant tensile stress specimens were selected for analysis: one was 0.8UTS right after yielding, and another was 0.9UTS, which well surpasses the yield strength. Both the fracture surface features showed a dimple zone at the center and a surrounding brittle zone between the specimen side surface and the perimeter of the dimple zone (Figure 6a,b). In the case of 0.9UTS, the brittle zone had an outer typical trans-granular cleavage-like region and an inner quasi-cleavage region. Widths of the cleavage-like region and quasi-cleavage region were 20–30 μm and 30–100 μm, respectively. At a lower applied stress 0.8UTS, the brittle zone became much wider, and the outer trans-granular cleavage-like region was replaced by an inter-granular fracture region (Figure 6c,d). The widths of the inter-granular fracture region and the quasi-cleavage region increased remarkably to 50–80 μm and 70–160 μm, respectively.

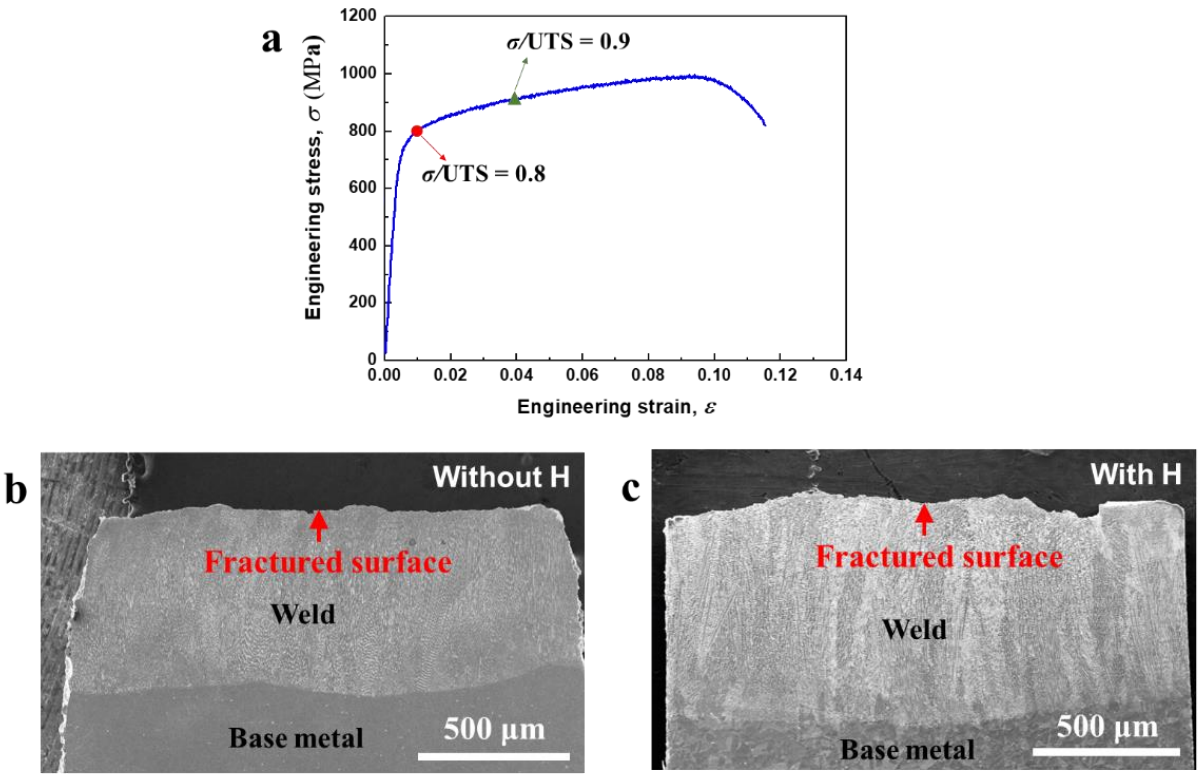

Figure 4. (**a**) Engineering stress–strain curve of a hydrogen-free weldment specimen. Fracture in the weld of the tensile weldment specimens of hydrogen-free (**b**) and hydrogen-charged (**c**).

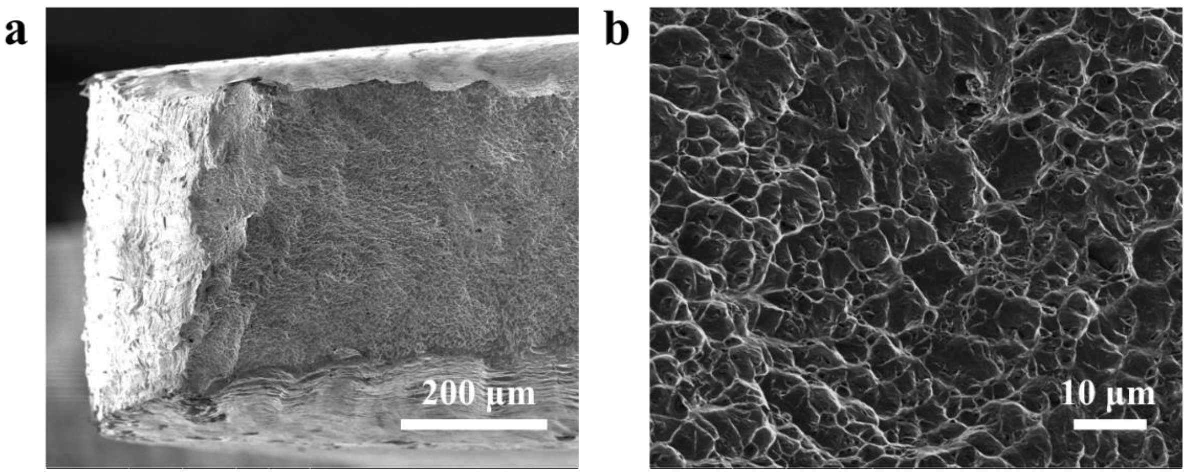

Figure 5. Topographical feature of the fractured surface of the hydrogen-free weldment tensile specimen tested at room temperature in air. (**a**) Macro morphology. (**b**) The dimple.

3.2. Central Dimple Zone

Figure 6e,f shows a zoomed-in view of the dimple zone of the hydrogen-charged specimens fractured at 0.9UTS and 0.8UTS. Most dimples of both specimens were 2–4 μm in diameter. A few large dimples were present and can be related to large inclusions (as indicated by the white arrows in Figure 6e). Particularly, no secondary crack was observed in the dimple zone when the applied stress was 0.9UTS. By contrast, many secondary cracks could be found in the dimple zone when the applied stress was 0.8UTS (as indicated by the green arrows in Figure 6f). These secondary cracks were 4–8 μm in length.

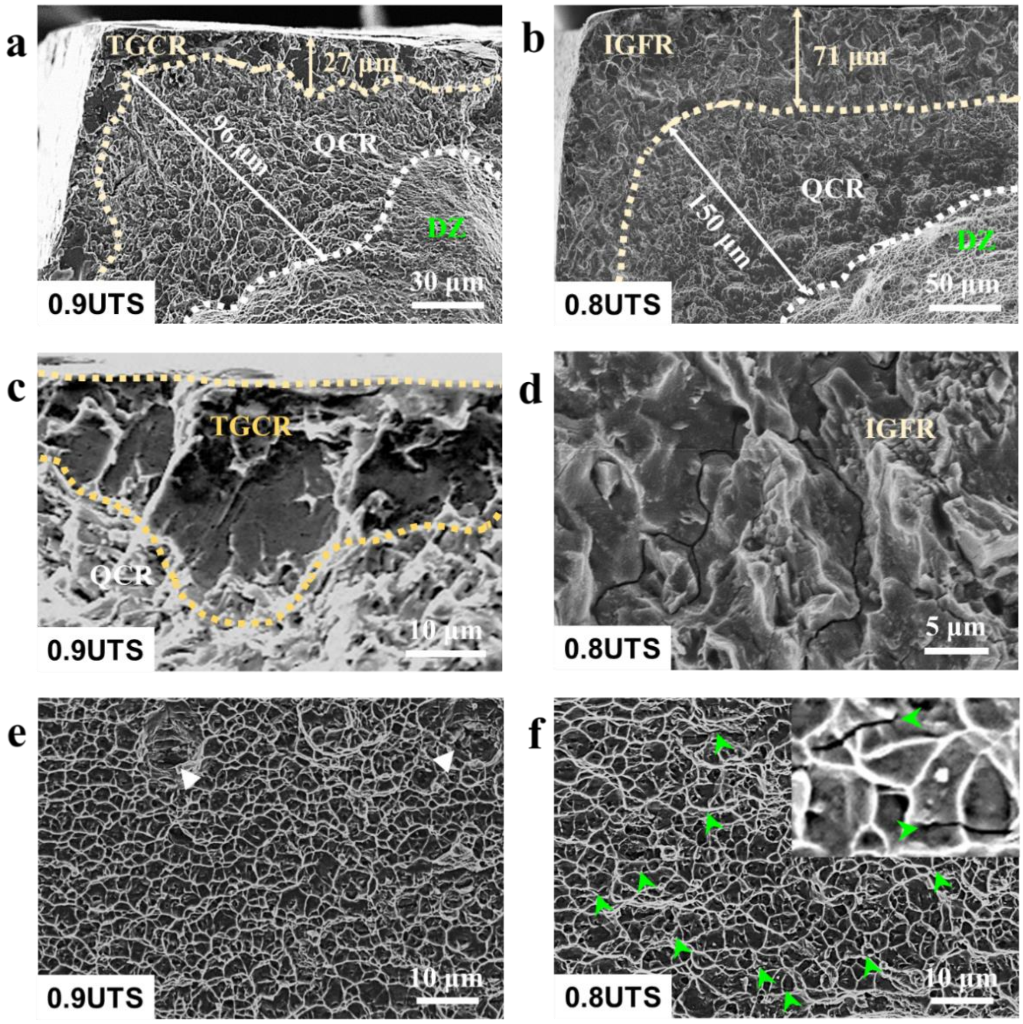

Figure 6. Topographical features of the fractured surfaces of the dynamic hydrogen-charging constant stress tensile specimens. (**a**,**c**,**e**) 0.9UTS-loaded specimen. (**b**,**d**,**f**) 0.8UTS-loaded specimen. DZ: dimple zone, QCR: quasi-cleavage region, TGCR: trans-granular cracking region, IGFR: inter-granular fracture region. White arrows in (**e**) indicate large dimples that can be correlated to large inclusions. Insert in (**f**) shows an enlarged image of the secondary cracks. Green arrows in (**f**) indicate secondary cracks.

4. Discussions

The hydrogen trap and transport by dislocations have been confirmed by numerous studies [34–39]. For the dynamic hydrogen-charged constant stress tensile specimens, when the applied stress is 0.9UTS, the corresponding plastic strain (ε) of the specimen is about 0.035 (see Figure 4a); therefore, significant dislocation is expected in the material that can transport and trap hydrogen atoms. To verify this, this work investigated the dislocation activities in a cracked thin film specimen of the material. As shown in Figure 7, the dislocations do not form slip bands, as commonly reported in the base metal, but tend to entangle locally in front of the crack tip, forming dislocation clouds. Furthermore, since hydrogen can facilitate the localization of plastic deformation [40,41], hydrogen can be transported by the dislocation activities and preferentially enrich in these dislocation clouds during the dynamic hydrogen charging [42]. These effects result in the preferential propagation of cleavage-like cracks within the grain [43–46]. Since hydrogen concentration is highest on the specimen surface and gradually diffuses into the interior of the specimen, such microscale cleavage-like cracking should have been evident in regions near the specimen side surface (as evidenced by Figure 6c).

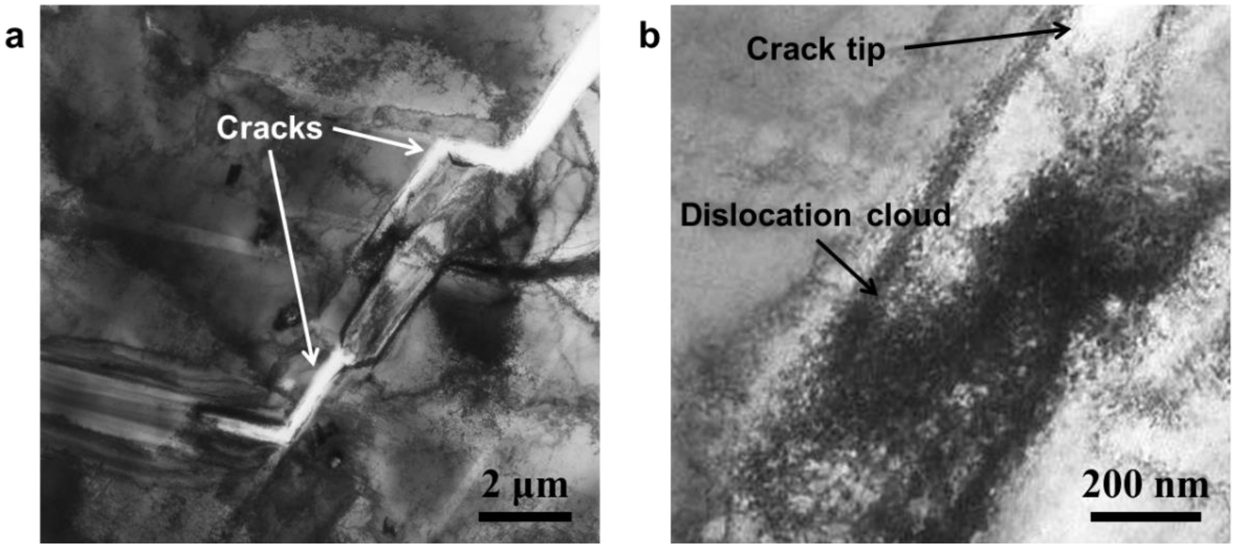

Figure 7. In situ transmission electron microscopy observation of the tensile deformation in a hydrogen-charged film specimen of the weld. (**a**) Dislocations do not reversely pile up in a planar manner in front of a propagating crack tip, but tend to entangle and form dislocation clouds. (**b**) Enlarged image of the dislocation cloud. It can be anticipated that these dislocation clouds would trap hydrogen and might facilitate local crack propagation under the high-stress state.

With the preferential nucleation of cracks near the side surface, the effective bearing area of the specimen decreased, rendering increasing global stress on the specimen cross-section. Driven by the increasing stress, the crack propagation is expected to speed up; and hydrogen diffusion from the surface is insufficient to fuel the above effects of hydrogen, and hence, brittle features on the fractured surface gradually disappear. This is clearly evidenced by the transition from cleavage-like cracking to quasi-cleavage cracking to eventually dimple fractures in the center of the specimen (see Figure 6a).

To further confirm this, finite element simulations were performed to illustrate the hydrogen distribution in the cross-section of the specimen (Figure 8). The calculation is based on the diffusion equation of hydrogen concentration, which is used to provide a semiquantitative estimation of hydrogen distribution. The simulated model size and diffusion coefficients [47] are adopted from the experiments. Figure 8a,b present the contour plot of the hydrogen distribution within the simulated specimens; as shown, the diffusion interface of the 0.9UTS-loaded specimen is much sharper than that of the 0.8UTS-loaded specimen, which is ascribed to a shorter diffusion time. The hydrogen concentration distribution along the horizontal direction in the specimen center is given in Figure 8c. Clearly, within the lifetime of the 0.9UTS-loaded specimen (Figure 8b), hydrogen is far from soaking the specimen (Figure 8a).

By contrast, when the applied stress is 0.8UTS, the corresponding plastic strain ε is much lower (~0.005, see Figure 4a), which means that the plastic deformation of the specimen was not significant. Therefore, microscale cleavage cracking promotion by dislocations is hindered. For the grains close to the specimen surface without dislocation slip, the hydrogen should be trapped preferentially at the grain boundaries. The enrichment of hydrogen on the grain boundaries would decrease their cohesive strength [48–54]. When the hydrogen concentration on the grain boundaries reached a critical value, local decohesion cracks initiated and propagated along the grain boundaries. Consequently, hydrogen-induced cracking along the grain boundaries led to dominant inter-granular fracture (Figure 6d).

Similarly, the formation of intergranular cracks near the surface reduces the effective bearing area of the specimen, and hence, increases the actual stress on the cross-section. Driven by the high stress and localized hydrogen concentration, non-trivial plastic deformation carried by dislocation activities is expected at the crack tip, resulting in cleavage-like and quasi-cleavage fracture beyond the inter-granular cracking region. As the cracks propagate into the interior of the specimen, hydrogen concentration near the crack tip decreases, together with the embrittlement effects, leading to eventual dimple fracture at the center of the specimen. This is further supported by the hydrogen concentration simulation (Figure 8b) that hydrogen is still not soaking the specimen within the lifetime of the 0.8UTS-loaded specimen. It should be noted that hydrogen concentration in the interior of the 0.8UTS-loaded specimen is obviously higher than that of the 0.9UTS-loaded specimen. Consistently, hydrogen embrittlement featured by secondary cracks is more evident in the 0.8UTS-loaded specimen.

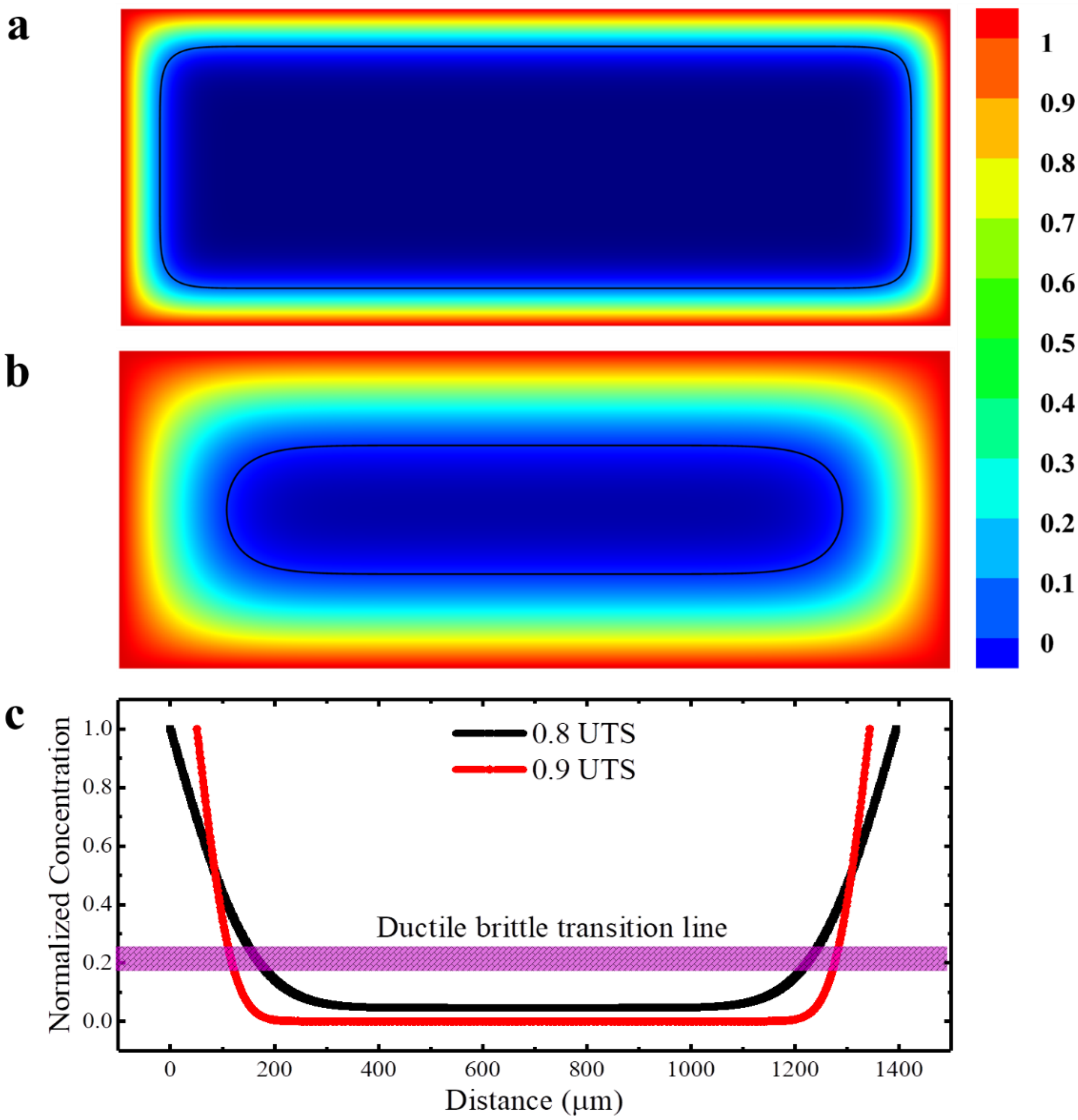

Figure 8. Simulated hydrogen distribution contour in the specimens at the fracture time. (**a**) At 361 h of 0.9UTS specimen, and (**b**) at 1941.5 h of 0.8UTS specimen, respectively. (**c**) The corresponding normalized hydrogen concentration along the horizontal direction in the specimen center. The dark line in Figure 6a,b, and the pink area in Figure 6c indicate the fracture interface.

5. Conclusions

In summary, the non-trivial influence of the applied stress on the mechanism of hydrogen embrittlement of JBK-75 alloy weldment was thoroughly interrogated. When the applied stress well surpassed the yield strength of the weld, the hydrogen-induced delayed fracture mode from the surface to the interior sequentially consisted of a trans-granular cleavage-like region, a quasi-cleavage region, and a dimple zone. With the applied stress decreased to close to the yield strength, inter-granular fracture was predominant near the surface. The critical role of dislocation activities and the competition of hydrogen diffusion and crack propagation in determining the cracking mode were revealed. The findings should, in principle, apply to many other austenite metals wherein hydrogen diffusion within the matrix is limited.

Author Contributions: Conceptualization, Y.Y. (Yingjie Yan), H.W., Y.H. and L.Q.; methodology, Y.Y. (Yingjie Yan), Y.C., R.C., H.W., Y.H., Y.Y. (Yu Yan) and L.Q.; software, H.W.; validation, Y.Y. (Yingjie Yan), R.C., H.W., Y.H., Y.Y. (Yu Yan) and L.Q.; formal analysis, Y.Z., L.Z., Y.C., R.C., Y.Y. (Yingjie Yan) and L.Q.; investigation, Y.Y. (Yu Yan), Y.Z. and L.Z.; data curation, Y.Y. (Yingjie Yan), Y.Z., L.Z. and Y.C.; writing—original draft preparation, Y.Y. (Yu Yan), Y.Z., L.Z. and Y.C.; writing—review and editing, Y.Y. (Yingjie Yan), H.W. and Y.H.; visualization, Y.Y. (Yu Yan) and Y.Z.; supervision, Y.Y. (Yingjie Yan), H.W., Y.H. and L.Q.; project administration, Y.Y. (Yingjie Yan) and R.C.; funding acquisition, Y.Y. (Yingjie Yan) and H.W. All authors have read and agreed to the published version of the manuscript.

Funding: This work was supported by the National Natural Science Foundation of China (51961024, 51901013, 52071170).

Institutional Review Board Statement: Not applicable.

Informed Consent Statement: Not applicable.

Data Availability Statement: No new data were created or analyzed in this study. Data sharing is not applicable to this article.

Conflicts of Interest: The authors declare no conflict of interest.

References

1. Zhong, W.; Cai, Y.; Tománek, D. Computer simulation of hydrogen embrittlement in metals. *Nature* **1993**, *362*, 435–437. [CrossRef]
2. Tiegel, M.C.; Martin, M.L.; Lehmberg, A.K.; Deutges, M.; Borchers, C.; Kirchheim, R. Crack and blister initiation and growth in purified iron due to hydrogen loading. *Acta Mater.* **2016**, *115*, 24–34. [CrossRef]
3. Kim, W.K.; Koh, S.U.; Yang, B.Y.; Kim, K.Y. Effect of environmental and metallurgical factors on hydrogen induced cracking of HSLA steels. *Corros. Sci.* **2008**, *50*, 3336–3342. [CrossRef]
4. Zan, N.; Ding, H.; Guo, X.F.; Tang, Z.Y.; Bleck, W. Effects of grain size on hydrogen embrittlement in a Fe-22Mn-0.6C TWIP steel. *Int. J. Hydrog. Energy* **2015**, *40*, 10687–10696. [CrossRef]
5. Hoyos, J.J.; Masoumi, M.; Pereira, V.F.; Tschiptschin, A.P.; Paes, M.T.P.; Avila, J.A. Influence of hydrogen on the microstructure and fracture toughness of friction stir welded plates of API 5L X80 pipeline steel. *Int. J. Hydrog. Energy* **2019**, *44*, 23458–23471. [CrossRef]
6. Saini, N.; Pandey, C.; Mahapatra, M.M. Effect of diffusible hydrogen content on embrittlement of P92 steel. *Int. J. Hydrog. Energy* **2017**, *42*, 17328–17338. [CrossRef]
7. Li, X.B.; Gao, M.; Li, H.Z.; Xing, W.W.; Zhang, L.; Shu, L.; Zhao, X.J.; Ma, Y.C.; Liu, K. Effect of residual hydrogen content on the tensile properties and crack propagation behavior of a type 316 stainless steel. *Int. J. Hydrog. Energy* **2019**, *44*, 25054–25063. [CrossRef]
8. Wang, M.Q.; Akiyama, E.; Tsuzaki, K. Determination of the critical hydrogen concentration for delayed fracture of high strength steel by constant load test and numerical calculation. *Corros. Sci.* **2006**, *48*, 2189–2202. [CrossRef]
9. Najam, H.; Koyama, M.; Bal, B.; Akiyama, E.; Tsuzaki, K. Strain rate and hydrogen effects on crack growth from a notch in a Fe-high-Mn steel containing 1.1wt% solute carbon. *Int. J. Hydrog. Energy* **2020**, *45*, 1125–1139. [CrossRef]
10. Momotani, Y.; Shibata, A.; Terada, D.; Tsuji, N. Effect of strain rate on hydrogen embrittlement in low-carbon martensitic steel. *Int. J. Hydrog. Energy* **2017**, *42*, 3371–3379. [CrossRef]
11. Zhou, C.S.; Song, Y.Y.; Shi, Q.Y.; Hu, S.Y.; Zheng, J.Y.; Xu, P.; Zhang, L. Effect of pre-strain on hydrogen embrittlement of metastable austenitic stainless steel under different hydrogen conditions. *Int. J. Hydrog. Energy* **2019**, *44*, 26036–26048. [CrossRef]

12. Fu, H.; Wang, W.; Zhao, H.Y.; Jin, F.; Li, J.X. Study of hydrogen-induced delayed fracture in high-Mn TWIP/TRIP steels during in situ electrochemical hydrogen-charging: Role of microstructure and strain rate in crack initiation and propagation. *Corros. Sci.* **2020**, *162*, 108191. [CrossRef]
13. Liu, H.W. Hydrogen assisted intergranular cracking in steels. *Eng. Fract. Mech.* **2011**, *78*, 2563–2571. [CrossRef]
14. Robertson, I.M.; Sofronis, P.; Nagao, A.; Martin, M.L.; Wang, S.; Gross, D.W.; Nygren, K.E. Hydrogen Embrittlement Understood. *Metall. Mater. Trans. B* **2015**, *46*, 1085–1103. [CrossRef]
15. Li, H.; Venezuela, J.; Qian, Z.; Zhou, Q.J.; Shi, Z.M.; Yan, M.; Knibbe, R.; Zhang, M.X.; Dong, F.T.; Atrens, A. Hydrogen fracture maps for sheared-edge-controlled hydrogen-delayed fracture of 1180 MPa advanced high-strength steels. *Corros. Sci.* **2021**, *48*, 109360. [CrossRef]
16. Rho, B.S.; Hong, H.U.; Nam, S.W. Analysis of the intergranular cavitation of Nb-A286 alloy in high temperature low cycle fatigue using EBSD technique. *Scr. Mater.* **2000**, *43*, 167–173. [CrossRef]
17. Zhao, M.J.; Guo, Z.F.; Rong, L.J. Effect of boron on the microstructure, mechanical properties and hydrogen performance in a modified A286. *Mater. Sci. Eng. A* **2010**, *527*, 5844–5851. [CrossRef]
18. Brooks, J.A.; Thompson, A.W. Microstructure and hydrogen effects on fracture in the alloy A-286. *Metall. Mater. Trans. A* **1993**, *24*, 1983–1991. [CrossRef]
19. Li, Y.Y.; Fan, C.G.; Rong, L.J.; Yan, D.S.; Li, X.Y. Hydrogen embrittlement resistance of austenitic alloys and aluminium alloys. *Acta. Metall. Sin.* **2010**, *46*, 1335–1346. [CrossRef]
20. Nakkalil, R.; Richards, N.L.; Chaturvedi, M.C. Fusion zone microstructure of electron beam welded incoloy 903. *Scr. Metall. Mater.* **1992**, *26*, 545–550. [CrossRef]
21. Richards, N.L.; Nakkalil, R.; Chaturvedi, M.C. The influence of electron-beam welding parameters on heat-affected-zone microfissuring in INCOLOY 903. *Metall. Mater. Trans. A* **1994**, *25*, 1733–1745. [CrossRef]
22. Tschegg, E.K.; Tauschitz, C.; Stanzl, S.E. The fatigue crack growth behavior of electron-beam welded a286 superalloy. *Metall. Mater. Trans. A* **1982**, *13*, 1483–1489. [CrossRef]
23. Mei, Y.P.; Liu, Y.C.; Liu, C.X.; Li, C.; Yu, L.M.; Guo, Q.Y.; Li, H.J. Effect of base metal and welding speed on fusion zone microstructure and HAZ hot-cracking of electron-beam welded Inconel 718. *Mater. Des.* **2016**, *89*, 964–977. [CrossRef]
24. Pereira, P.A.S.; Franco, C.S.G.; Filho, J.L.M.G.; Santos, D.S.d. Hydrogen effects on the microstructure of a 2.25Cr–1Mo–0.25 V steel welded joint. *Int. J. Hydrog. Energy* **2015**, *40*, 17136–17143. [CrossRef]
25. Zafra, A.; Belzunce, J.; Rodríguez, C.; Fernández-Pariente, I. Hydrogen embrittlement of the coarse grain heat affected zone of a quenched and tempered 42CrMo4 steel. *Int. J. Hydrog. Energy* **2020**, *45*, 16890–16908. [CrossRef]
26. Oliveira, J.P.; Crispim, B.; Zeng, Z.; Omori, T.; Fernandes, F.M.B.; Miranda, R.M. Microstructure and mechanical properties of gas tungsten arc welded Cu-Al-Mn shape memory alloy rods. *J. Mater. Process. Tech.* **2019**, *271*, 93–100. [CrossRef]
27. Yang, J.; Oliveira, J.P.; Li, Y.L.; Tan, C.W.; Gao, C.K.; Zhao, Y.X.; Yu, Z.S. Laser techniques for dissimilar joining of aluminum alloys to steels: A critical review. *J. Mater. Process. Tech.* **2022**, *301*, 117443. [CrossRef]
28. Oliveira, J.P.; Shamsolhodaei, A.; Shen, J.J.; Lopes, J.G.; Gonçalves, R.M. Improving the ductility in laser welded joints of CoCrFeMnNi high entropy alloy to 316 stainless steel. *Mater. Des.* **2022**, *219*, 110717. [CrossRef]
29. Chen, S.H.; Zhao, M.J.; Liang, H.; Rong, L.J. Microstructure and Mechanical Properties of Electron Beam Welded Alloy J75. *J. Mater. Sci. Technol.* **2014**, *30*, 493–498. [CrossRef]
30. Chen, S.H.; Hu, H.L.; Zhao, M.J.; Rong, L.J. Effect of post-weld aging treatment on the precipitation and mechanical behavior of Fe-Ni based alloy weldment. *Mater. Sci. Eng. A* **2018**, *718*, 363–370. [CrossRef]
31. Yan, Y.J.; Yan, Y.; He, Y.; Li, J.X.; Su, Y.J.; Qiao, L.J. The mechanism of precipitation strengthening in Fe–Ni austenitic alloy electron beam weldment. *Mater. Sci. Eng. A* **2015**, *630*, 85–89. [CrossRef]
32. Yan, Y.J.; Yan, Y.; He, Y.; Li, J.X.; Su, Y.J.; Qiao, L.J. Hydrogen-induced cracking and service safety evaluation for precipitation strengthened austenitic stainless steel as hydrogen storage tank. *Int. J. Hydrog. Energy* **2014**, *39*, 17921–17928. [CrossRef]
33. Xu, J.; Sun, X.K.; Chen, W.X.; Li, Y.Y. Hydrogen permeation and diffusion in iron-base superalloys. *Acta Metall. Mater.* **1993**, *41*, 1455–1459. [CrossRef]
34. Liu, Y.; Wang, M.Q.; Liu, G.Q. Hydrogen trapping in high strength martensitic steel after austenitized at different temperatures. *Int. J. Hydrog. Energy* **2013**, *38*, 14364–14368. [CrossRef]
35. Phaniraj, M.P.; Kim, H.J.; Suh, J.Y.; Shim, J.H.; Park, S.J.; Lee, T.H. Hydrogen embrittlement in high interstitial alloyed 18Cr10Mn austenitic stainless steels. *Int. J. Hydrog. Energy* **2015**, *40*, 13635–13642. [CrossRef]
36. Chen, S.H.; Zhao, M.J.; Rong, L.J. Role of gamma' characteristic on the hydrogen embrittlement susceptibility of Fe-Ni-Cr alloys. *Corros. Sci.* **2015**, *101*, 75–83. [CrossRef]
37. Zhang, Z.B.; Moore, K.L.; McMahon, G.; Morana, R.; Preuss, M. On the role of precipitates in hydrogen trapping and hydrogen embrittlement of a nickel-based superalloy. *Corros. Sci.* **2019**, *146*, 58–69. [CrossRef]
38. Cheng, X.Y.; Zhang, H.X. A new perspective on hydrogen diffusion and hydrogen embrittlement in low-alloy high strength steel. *Corros. Sci.* **2020**, *174*, 108800. [CrossRef]
39. Dong, L.S.; Wang, S.Z.; Wu, G.L.; Gao, J.H.; Zhou, X.Y.; Wu, H.H.; Mao, X.P. Application of atomic simulation for studying hydrogen embrittlement phenomena and mechanism in iron-based alloys. *Int. J. Hydrog. Energy* **2022**, *47*, 20288–20309. [CrossRef]
40. Sofronis, P.; Birnbaum, H.K. Mechanics of the hydrogen-dislocation-impurity interactions—I. Increasing shear modulus. *J. Mech. Phys. Solids* **1995**, *43*, 49–90. [CrossRef]

41. Robertson, I.M.; Birnbaum, H.K.; Sofronis, P. Chapter 91 Hydrogen Effects on Plasticity. *Dislocat. Solids* **2009**, *15*, 249–293. [CrossRef]
42. Pundt, A.; Kirchheim, R. Hydrogen in metals: Microstructural aspects. *Annu. Rev. Mater. Res.* **2006**, *36*, 555–608. [CrossRef]
43. Robertson, I.M.; Birnbaum, H.K. An HVEM study of hydrogen effects on the deformation and fracture of nickel. *Acta Metall.* **1986**, *34*, 353–366. [CrossRef]
44. Neeraj, T.; Srinivasan, R.; Li, J. Hydrogen embrittlement of ferritic steels: Observations on deformation microstructure, nanoscale dimples and failure by nanovoiding. *Acta Mater.* **2012**, *60*, 5160–5171. [CrossRef]
45. Martin, M.L.; Fenske, J.A.; Liu, G.S.; Sofronis, P.; Robertson, I.M. On the formation and nature of quasi-cleavage fracture surfaces in hydrogen embrittled steels. *Acta Mater.* **2011**, *59*, 1601–1606. [CrossRef]
46. Nibur, K.A.; Somerday, B.P.; Balch, D.K.; Marchi, C.S. The role of localized deformation in hydrogen-assisted crack propagation in 21Cr–6Ni–9Mn stainless steel. *Acta Mater.* **2009**, *57*, 3795–3809. [CrossRef]
47. Zhou, X.Y.; Zhu, J.H.; Wu, Y.; Yang, X.S.; Lookman, T.; Wu, H.H. Machine learning assisted design of FeCoNiCrMn high-entropy alloys with ultra-low hydrogen diffusion coefficients. *Acta Mater.* **2022**, *224*, 117535. [CrossRef]
48. Oudriss, A.; Creus, J.; Bouhattate, J.; Conforto, E.; Berziou, C.; Savall, C.; Feaugas, X. Grain size and grain-boundary effects on diffusion and trapping of hydrogen in pure nickel. *Acta Mater.* **2012**, *60*, 6814–6828. [CrossRef]
49. Chen, Y.S.; Lu, H.Z.; Liang, J.T.; Rosenthal, A.; Liu, H.W.; Sneddon, G.; McCarroll, I.; Zhao, Z.Z.; Li, W.; Guo, A.M.; et al. Observation of hydrogen trapping at dislocations, grain boundaries, and precipitates. *Science* **2020**, *367*, 171–175. [CrossRef]
50. Alvaro, A.; Jensen, I.T.; Kheradmand, N.; Løvvik, O.M.; Olden, V. Hydrogen embrittlement in nickel, visited by first principles modeling, cohesive zone simulation and nanomechanical testing. *Int. J. Hydrog. Energy* **2015**, *40*, 16892–16900. [CrossRef]
51. Li, X.F.; Zhang, J.; Akiyama, E.; Wang, Y.F.; Li, Q.Z. Microstructural and crystallographic study of hydrogen-assisted cracking in high strength PSB1080 steel. *Int. J. Hydrog. Energy* **2018**, *43*, 17898–17911. [CrossRef]
52. Okada, K.; Shibata, A.; Takeda, Y.; Tsuji, N. Crystallographic feature of hydrogen-related fracture in 2Mn-0.1C ferritic steel. *Int. J. Hydrog. Energy* **2018**, *43*, 11298–11306. [CrossRef]
53. Kim, K.S.; Kang, J.H.; Kim, S.J. Carbon effect on hydrogen diffusivity and embrittlement in austenitic stainless steels. *Corros. Sci.* **2020**, *180*, 109226. [CrossRef]
54. Zhou, X.Y.; Zhu, J.H.; Wu, H.H.; Yang, X.S.; Wang, S.Z.; Mao, X.P. Unveiling the role of hydrogen on the creep behaviors of nanograined α-Fe via molecular dynamics simulations. *Int. J. Hydrog. Energy* **2021**, *46*, 9613–9629. [CrossRef]